Atomistic Mechanisms for the Nucleation of Aluminum Oxide Nanoparticles

5 AUTHORS, INCLUDING:

Julien Lam
University of Bristol
7 PUBLICATIONS **8** CITATIONS

Christophe Dujardin
Claude Bernard University Lyon 1
234 PUBLICATIONS **2,911** CITATIONS

G. Ledoux
Claude Bernard University Lyon 1
129 PUBLICATIONS **2,606** CITATIONS

Abdul-Rahman Allouche
Claude Bernard University Lyon 1
162 PUBLICATIONS **2,100** CITATIONS

Atomistic Mechanisms for the Nucleation of Aluminum Oxide Nanoparticles

Julien Lam,* David Amans,* Christophe Dujardin, Gilles Ledoux, and Abdul-Rahman Allouche

Université Lyon 1, F-69622 Villeurbanne, France, UMR5306 CNRS, Institut Lumiere Matiere, PRES-Université de Lyon, F-69361 Lyon, France

S *Supporting Information*

ABSTRACT: A predictive model for nanoparticle nucleation has not yet been successfully achieved. Classical nucleation theory fails because the atomistic nature of the seed has to be considered. Indeed, geometrical structure as well as stoichiometry do not always match the bulk values. We present a fully microscopic approach based on a first-principle study of aluminum oxide clusters. We calculated stable structures of Al_xO_y and their associated thermodynamic properties. From these data, the chemical composition of a gas composed of aluminum and oxygen atoms can be calculated as a function of temperature, pressure, and aluminum to oxygen ratio. We demonstrate the accuracy of this approach in reproducing experimental results obtained with time-resolved spectroscopy of a laser-induced plasma from an Al_2O_3 target. We thus extended the calculation to lower temperatures, i.e., longer time scales, to propose a scenario of composition gas evolution leading to the first alumina seeds.
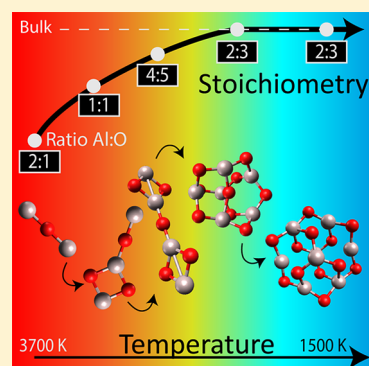
INTRODUCTION

Although the nucleation of nanoparticles is of crucial interest for a wide range of applications, such as the nanoparticle synthesis or the fight against atmospheric nanoparticles, a predictive model of its mechanisms is not yet achieved. Nucleation consists of the formation of a more stable seed within a metastable phase. This phenomenon can be observed in any first-order phase transition especially with vapor-phase condensation, liquid-to-vapor boiling, solid-state precipitation, and binary separations.[1−4] Since the beginning of the 19th century, classical nucleation theory (CNT) has been used for intuitive descriptions.[5−7] The CNT describes the formation of a spherical particle immersed in a mother phase as a competition between the volume and the surface energies, whereas ΔG_v, the standard Gibbs free energy difference per unit volume between the two phases favors the growth, the surface term, proportional to the surface tension σ, has an opposite effect. As a result, CNT states the existence of a minimum radius r^* allowing the new phase to grow for radii larger than r^*. r^* is defined by[3]

$$r^* = -\frac{2\sigma}{\Delta G_v} \tag{1}$$

CNT appears to be successful for liquid nucleation in a supersaturated vapor.[8,9] However, this approach remains controversial regarding quantitative results,[10−13] and its conceptual limitations have been raised by several authors.[10,13−15] On the one hand, CNT assumes that the seed is homogeneous and isostructural to the bulk crystal. On the other hand, the Otswald rule[16−18] states that the first growing phase is not always the most stable. During the crystal growth, the geometric structure may indeed reorganize with transient

states potentially having a different structure from the bulk analog.[19,20] A second limitation of CNT arises from the capillary approximation which assumes that nucleus and bulk materials have the same thermodynamic properties, and particularly the same surface tension. As an illustration, one may consider the case of Al_2O_3. For both crystallographic phases (α and γ), σ is almost 1.5 J m^{-2} for nanoparticles[21] and ΔG_v is almost −62 kJ cm^{-3} at 298 K.[22] CNT predicts a critical radius of about the Bohr radius. Lastly, the nucleation rate is driven by the probability of a seed reaching r^* by addition of molecules.[5,6] This approach involves parameters difficult to quantify.[23] Consequently, the CNT usually fails to predict the nucleation rate, with tens of orders of magnitude discrepancy between theory and experiment.[13]

Over and beyond the CNT's limitations, the need to explore crystal nucleation becomes increasingly crucial because it may provide a control on the crystal structure and size distribution for nanoparticle synthesis.[24] Experimentally, it is challenging to probe nucleation processes because it involves time and length scales that are usually too fast and too small in most experiments.

For computer simulations, two trends can be identified in the literature. On the one hand, molecular dynamics calculations are used with hard-sphere,[25] Lennard-Jones[9,26,27] or more refined potentials[23,28−30] to investigate the nucleation kinetics. On the other hand, first principle calculations are used to study with precision clusters for particular systems such as zinc,[31] silicon,[32] and titanium[33,34] oxides. Apart from the work of

Loschen et al.[35] who tested different stoichiometries of cerium oxides only the bulk stoichiometry is generally considered in simulations. In addition, very few works compared these computational results with experimental measurements.[36]

Our work is carried out in the context of laser ablation, including pulsed laser deposition[37] or pulsed laser ablation in liquids.[38,39] But it can be generalized to other methods such as cluster sources[40] and gas-phase combustion.[41] For all these techniques, an atomic vapor or a plasma is generated at temperatures higher than a thousand Kelvins. Then, the system is quenched down to room temperature, leading to nucleation and growth of the nanoparticles. We investigate nucleation processes through an original use of different tools from quantum chemistry combined with experimental measurements obtained from laser-induced plasma spectroscopy.[42] We choose to work with a model system made of aluminum and oxygen atoms. We first compute the lowest energy structures of Al_xO_y molecules. Thereafter, we calculate the gas-phase equilibrium composition as a function of the temperature, the pressure, and the initial ratio of aluminum to oxygen atoms. For the highest temperatures, the computed composition is compared to experimental measurements obtained from the laser ablation of an alumina target (α-Al_2O_3). Moreover, plasma spectroscopy allows the probing of short time scales, when the plasma is still hot and optically active.

■ NUMERICAL CALCULATIONS

Figure 1 reviews schematically the computational algorithm used for the structural investigation. For each value of x and y,
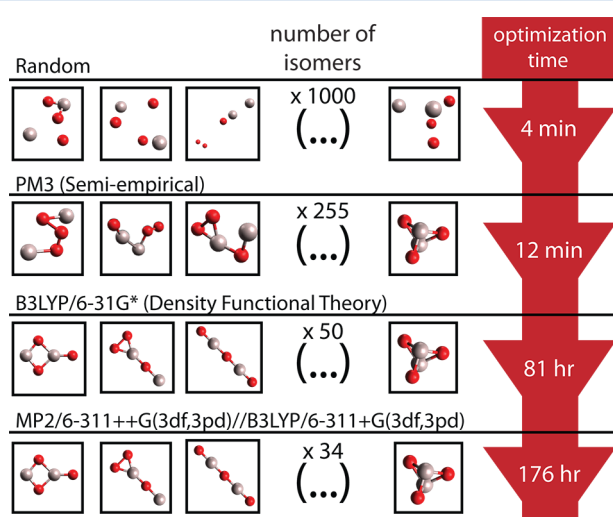
Figure 1. Computational optimization algorithm illustrated by the example of Al_2O_3 molecules. After each step, similar geometries are removed. The number of remaining geometries is indicated above the brackets. The time corresponds to the computational time for each step.

we start from a set of 1000 geometries where atoms are randomly disposed with interatomic distances corresponding to the covalent bond distances. The system is then relaxed via a PM3 semiempirical method.[43] The remaining geometries are then optimized using density functional theory (DFT) calculation. Two sets of bases are used successively, B3LYP/6-31G* and B3LYP/6-311+G(3df,3pd). The Gibbs energies were determined using MP2 and B3LYP according to the following steps. The harmonic frequencies were calculated by

B3LYP/6-311+G(3df,3pd) using the structures optimized. MP2 thermochemistry was determined by adding B3LYP thermal correction factors to the MP2 single-point energies and is reported as MP2/6-311++G(3df,3pd)//B3LYP/6-311+G(3df,3pd).

The dissociated geometries are removed and only geometries whose energy is at most 2 eV higher than the ground state are kept as the others are not relevant for the temperatures studied. For the biggest clusters $(Al_2O_3)_3$ and $(Al_2O_3)_4$, the structures published by Sharipov et al.[44] were used as inputs in our optimization process. DFT and MP2 calculations were performed with the Gaussian09 D01 revision.[45]

We investigated all the molecular formulas following $(x, y) \in [1; 4]$. In addition, two stoichiometric trends were followed, $(AlO)_n$ and $(Al_2O_3)_n$. $(AlO)_n$ with $n \leqslant 8$ were chosen because Patzer et al. demonstrated that for clusters with x and y smaller than 4, this stoichiometry is the most stable.[46] $(Al_2O_3)_n$ with $n \leqslant 4$ were investigated because it corresponds to the bulk stoichiometry.

Figure 2 shows the most stable structures we obtained. Point-zero energies and geometrical parameters can be found in the Supporting Information (SI.1). The method we used provides a systematic procedure to select the different stable chemical structures for a given molecular formula. Indeed, for some of
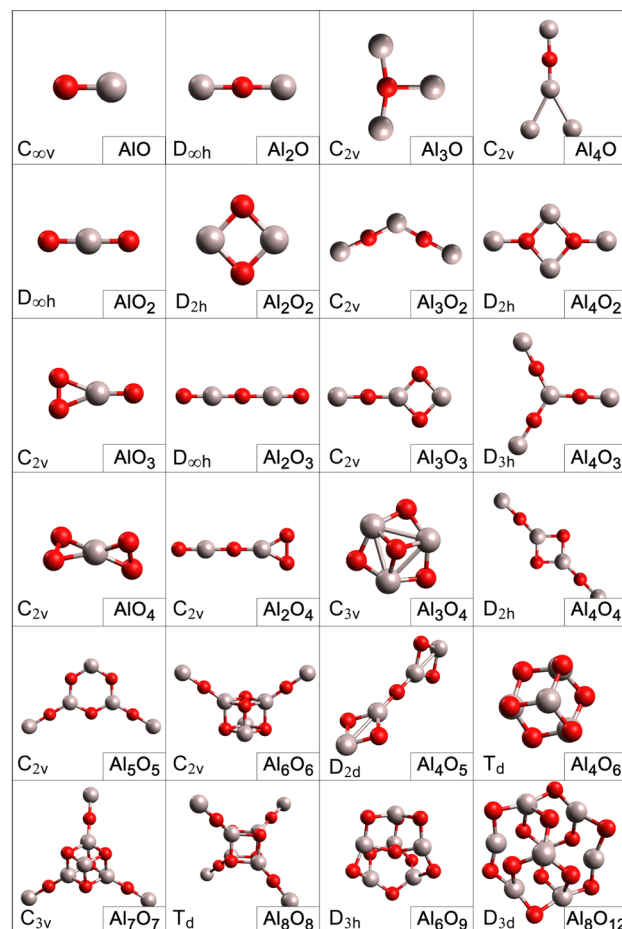
Figure 2. Most stable structures obtained at MP2/6-311++G-(3df,3pd)//B3LYP/6-311+G(3df,3pd) level of theory. The gray spheres and the red spheres correspond respectively to the aluminum atoms and the oxygen atoms.

the molecules, the results are consistent with various works published previously.[44,46,47] Nevertheless, for others such as AlO_4 and Al_2O_3, we were able to find isomers that are more stable than those obtained earlier.

The first principle calculations provide dissociation energy, vibrational, and rotational constants for all $Al_xO_y^{(i)}$ molecules, where i denotes an isomer of the molecular formula Al_xO_y. The formation Gibbs free energy $\Delta_f G_{Al_xO_y^{(i)}}$ of each $Al_xO_y^{(i)}$ is then computed as a function of the temperature T and the pressure $P°$. The Gibbs free energy calculation is described in Supporting Information SI.2. On the basis of the model proposed by Patzer et al.,[46] we computed the composition of a gas fed with aluminum and oxygen atoms as a function of the temperature, the initial proportion of elements ($\lambda \equiv N_{Al}/N_O$) and the pressure. We considered the set of reactions that correspond to the formation of the $Al_xO_y^{(i)}$ molecules from an atomic gas:

$$x\text{Al} + y\text{O} \rightleftarrows Al_xO_y^{(i)} \qquad (2)$$

The Gibbs free energy of reactions $\Delta_r G_{Al_xO_y^{(i)}}$ is deduced from the $\Delta_f G_{Al_xO_y^{(i)}}$.[48] We improved Patzer's model by taking into account the temperature and pressure dependences of $\Delta_r G_{Al_xO_y^{(i)}}$ and the contribution of all isomers for each molecules (Supporting Information SI.2).

■ EXPERIMENTAL DATA

The experimental measurements used for this work have been published previously[49] and are sketched in Figure 3. To summarize, we performed the spectroscopic characterization of a plasma
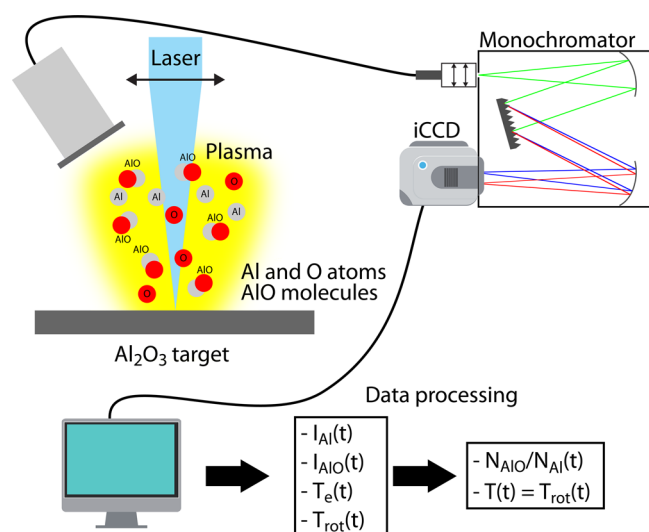
Figure 3. Sketch summarizing the experimental method: (i) a pulsed laser is focused onto an Al_2O_3 solid target generating an optically active plasma, (ii) the emitted light is recorded using a monochromator and an intensified CCD, (iii) Al and AlO intensities are obtained along with T_e and T_{rot} as a function of the time, (iv) intensities are corrected leading to a ratio in density.

induced by the laser ablation of an Al_2O_3 target in ambient air. The emission intensity of aluminum monoxide molecules and aluminum atoms was measured as a function of time. The electronic temperature T_e was also measured.[49] Using the formalisms developed in our previous article,[39] we deduced the density ratio N_{AlO}/N_{Al}. In the meantime, we measured

a temporal evolution of the rotational temperature T_{rot}. This can account for the temperature used in the thermochemistry model because the rotational temperature probes the kinetic temperature of atoms.[49] N_{AlO}/N_{Al} is then reported in Figure 4a not only as a function of the time (bottom axis)
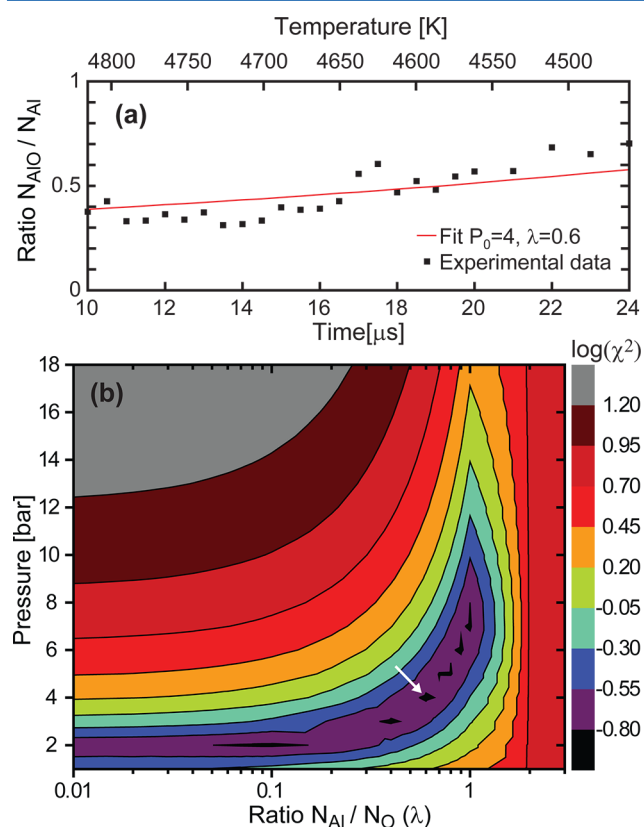
Figure 4. (a) The black squares correspond to the ratio N_{AlO}/N_{Al} measured as a function of time (bottom axis) and temperature (top axis). The solid line corresponds to the best fit, for $P° = 4$ bar and $\lambda = N_{Al}/N_O = 0.6$, deduced from the smallest figure of merit reported in panel (b). Numerical results for different values of λ and $P°$ are shown in Supporting Information SI.4. (b) Likelihood between the experimental ratio N_{AlO}/N_{Al} reported in the panel (a) and the theoretical ratio is given as a function of the ambient pressure $P°$ and the stoichiometry λ. The color bar shows the χ^2 values in logarithmic scale. The white arrow shows the minimum value of the χ^2.

but also as a function of the temperature T_{rot} (top axis). These experimental data will be used to validate the thermochemistry model.

The λ ratio is expected to be between two extreme values. $\lambda_{max} = 2/3$ corresponds to a plasma only composed of the ablated matter. λ_{min} corresponds to the ablated matter combined with the ambient air in the same plasma plume volume. The amount of matter ablated is obtained from the crater shape. The crater depth is measured by using Alpha-Step D100 profiler from Tencor. The crater depth measured after 5 pulses is 1.5 μm $\pm$ 500 nm. The crater diameter is measured with an optical microscope. The crater diameter is 500 μm $\pm$ 100 μm. Assuming an α-Al_2O_3 density of 3.95 g cm^{-3}, a molar mass of 101.96 g mol^{-1}, we have obtained $7 \times 10^{15} \pm 70\%$ atoms ablated per pulse. Considering the size of the plasma, 2 mm in diameter,[49] and assuming an ideal gas, the number of O_2 molecules contained in the same volume of air is 2×10^{16}.

The ratio between the number of aluminum atoms provided by the target and the number of oxygen atoms provided by the target and the air leads to a λ_{min} of 0.06 (Supporting Information SI.3).

■ DISCUSSION

In Figure 4b, the experimental measurements from 10 to 24 μs are compared with our calculations using the chi-squared test ($\chi^2 = \sum(X_{th} - X_{exp})^2$). We emphasis the valley of highest likelihood that exhibits a minimum of χ^2 for $P^\circ = 4$ bar and $\lambda = 0.6$. The λ value is consistent with the expected one. The deduced pressure is also consistent with previous plasma spectroscopy measurements.[50] Assuming these values, the theoretical ratio N_{AlO}/N_{Al} is computed as a function of the temperature and compared to the experimental data in Figure 4a. The agreement between theoretical calculation and experimental data relies on the idea that the plasma follows a quasi-static cooling in the considered time-range. The cooling rate measured is 25 K μs^{-1}. The known kinetics of the chemical reactions leading to oxide molecules[51] are fast enough to follow this cooling rate. This result is also consistent with the absence of an energy barrier for the reactions Al + O → AlO and Al + O_2 → AlO + O.[52] However, to assert equilibrium in the reacting gas, it could be relevant to take into account the homogeneity and the diffusion properties of the gas.

On the basis of the consistency between experimental and numerical results, we extended the thermochemistry calculation to lower temperature considering $P^\circ = 4$ bar and $\lambda = 0.6$. Figure 5 shows the gas composition as a function of the
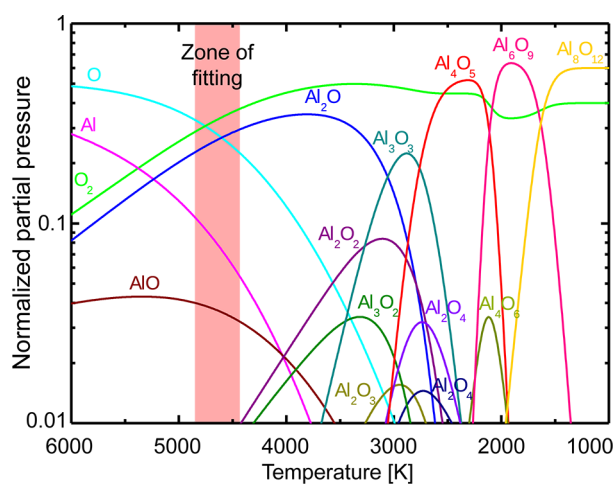
Figure 5. Evolution of the gas-phase composition from 6000 to 1000 K considering $P^\circ = 4$ bar and $\lambda = 0.6$. For clarity, the total pressure is normalized to one for each temperature. The partial pressure $P_{Al_xO_y}$ for a given x and a given y corresponds to the summation over all isomers.

temperature. Here, the partial pressure $P_{Al_xO_y}$ for a given molecular formula corresponds to the summation over all isomers partial pressure. As expected, at high temperature ($T \gtrsim 5000$ K), i.e., short times, the gas is mainly composed of the smallest species, i.e., Al, O, O_2, AlO, and Al_2O. Later, the amounts of Al_2O and O simultaneously decrease, leading to the two derivatives Al_2O_2 and Al_3O_3. We emphasize that Al_2O_3 never seems to emerge at this stage. The stoichiometry of
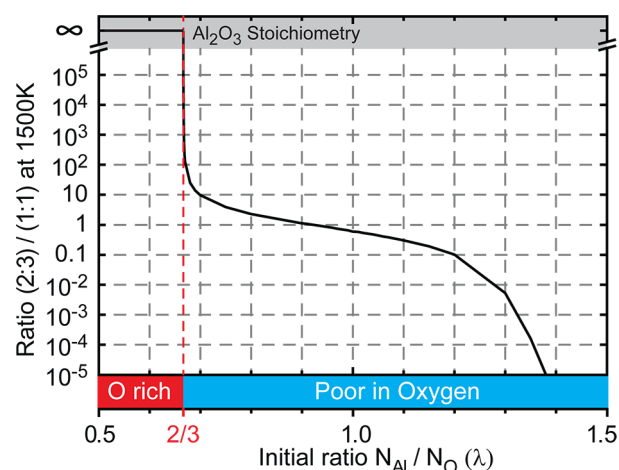
Figure 6. Ratio in pressure between molecules following $(Al_2O_3)_n$ and those following $(AlO)_n$ as a function of λ calculated at 1500 K. The full curve is shown in Supporting Information SI.5.

alumina, corresponding to Al_6O_9 and Al_8O_{12} molecules, emerges only for temperatures lower than 2000 K. In Figure 6, we observe a drastic dependence of the final composition for λ varying around 2/3. It indicates that a small excess of oxygen is required to favor the (2:3) stoichiometry. This result is consistent with the general idea that to synthesize oxides, it is required to use an oxygen-rich gas with respect to the stoichiometry. For example, plasma enhanced chemical vapor deposition (PECVD) uses an oxygen plasma to grow layers of oxides.[53,54] Pulsed laser deposition (PLD) of Al_2O_3 has been performed in an oxygen gas atmosphere to enhance the stoichiometry of the layer.[55] O_2 is injected during the growth of ZnO nanoparticles in low energy cluster beam deposition experiment (LECBD).[56]

■ CONCLUSIONS

In summary, first principle calculations were employed to investigate aluminum oxide clusters at different stoichiometries. A systematic optimization approach was followed to obtain the stable structures. We find more stable isomers than the previously published ones for AlO_4 and Al_2O_3 molecules.[46] Temperature evolution of the composition of a gas made of aluminum and oxygen atoms was also calculated using these molecular properties. Although for high temperature, $(AlO)_n$ is the most preponderant structure, the bulk aluminum oxide stoichiometry (2:3) starts to exceed the (1:1) stoichiometry for temperature lower than 2000 K. Besides the equilibrium considerations, the question of the kinetic of chemical reactions is not addressed here. Indeed, the occurrence of an equilibrium condition has to be combined with reasonable time scales of reaction kinetics to ensure the molecule formation. Especially, at low temperature, plasma spectroscopy can no longer provide the chemical composition because the system does not emit light. Nevertheless, the theoretical absorption and emission spectra can be deduced from our first-principles calculations. Laser-induced fluorescence will be performed to probe the gas. Finally, the high level of theory employed in our calculations prevents addressing bigger clusters. A complementary work could consist of using the clusters we obtained to parametrize a semiempirical model and perform molecular dynamics simulations. We were nevertheless able to predict the requirements for an oxygen rich gas for synthetizing the desired oxide stoichiometry.

■ ASSOCIATED CONTENT

Ⓢ Supporting Information

The Supporting Information is available free of charge on the ACS Publications website at DOI: 10.1021/acs.jpca.5b05829.

The geometry of each isomer is reported in xyz format (see section SI.1 of the pdf for content description) (ZIP)

Section SI.1 describes the content of the xyz files. Section SI.2 gives the formulas used to calculate the Gibbs free energy and the gas composition. Section SI.3 describes the λ_{min} calculation. The ratio N_{AlO}/N_{Al} is computed for different values of λ and $P°$ in section SI.4. The full curve corresponding to the Figure 6 is shown in section SI.5 (PDF)

■ AUTHOR INFORMATION

Corresponding Authors

*J. Lam. E-mail: julien.lam@univ-lyon1.fr.
*D. Amans. E-mail: david.amans@univ-lyon1.fr.

Notes

The authors declare no competing financial interest.

■ ACKNOWLEDGMENTS

■ REFERENCES

(1) Ford, I. J. Statistical Mechanics of Nucleation: A Review. *Proc. Inst. Mech. Eng., Part C* **2004**, *218*, 883−899.

(2) Clouet, E. Modeling of Nucleation Processes. *ArXiv e-prints* **2010**, arXiv:1001.4131.

(3) Abraham, F. F. *Homogeneous Nucleation Theory; The Pretransition Theory of Vapor Condensation (Advances in theoretical chemistry. Supplement)*; Academic Press: New York, 1973.

(4) Schmelzer, J. W. P., Ed. *Nucleation Theory and Applications*, 1st ed.; Wiley-VCH: New York, 2005.

(5) Volmer, M.; Weber, A. Germ-Formation in Oversaturated Figures. *Z. phys. chem.* **1926**, *119*, 277−301.

(6) Farkas, L. The Speed of Germinitive Formation in Over Saturated Vapours. *Z. Phys. Chem.* **1927**, *125*, 236−242.

(7) Becker, R.; Doring, W. Kinetic Treatment of Germ Formation in Supersaturated Vapour. *Ann. Phys.* **1935**, *416*, 719−752.

(8) Strey, R.; Wagner, P. E.; Viisanen, Y. The Problem of Measuring Homogeneous Nucleation Rates and the Molecular Contents of Nuclei: Progress in the Form of Nucleation Pulse Measurements. *J. Phys. Chem.* **1994**, *98*, 7748−7758.

(9) Diemand, J.; Angelil, R.; Tanaka, K. K.; Tanaka, H. Direct Simulations of Homogeneous Bubble Nucleation: Agreement with Classical Nucleation Theory and no Local Hot Spots. *Phys. Rev. E* **2014**, *90*, 052407.

(10) Viisanen, Y.; Strey, R.; Reiss, H. Homogeneous Nucleation Rates of Water. *J. Chem. Phys.* **1993**, *99*, 4680−4692.

(11) Viisanen, Y.; Strey, R. Homogeneous Nucleation Rates of n-Butanol. *J. Chem. Phys.* **1994**, *101*, 7835−7843.

(12) Hruby, J.; Viisanen, Y.; Strey, R. Homogeneous Nucleation Rates for n-Pentanol in Argon: Determination of the Critical Cluster Size. *J. Chem. Phys.* **1996**, *104*, 5181−5187.

(13) Sen, S.; Mukerji, T. A Generalized Classical Nucleation Theory for Rough Interfaces: Application in the Analysis of Homogeneous Nucleation in Silicate Liquids. *J. Non-Cryst. Solids* **1999**, *246*, 229−239.

(14) Lutsko, J. F.; Duran-Olivencia, M. A. Classical Nucleation Theory from a Dynamical Approach to Nucleation. *J. Chem. Phys.* **2013**, *138*, 244908.

(15) Lutsko, J. F.; Durán-Olivencia, M. A. A Two-Parameter Extension of Classical Nucleation Theory. *J. Phys.: Condens. Matter* **2015**, *27*, 235101.

(16) Ostwald, W. Studien über die Bildung und Umwandlung fester Körper. *Z. Phys. Chem.* **1897**, *22*, 289−330.

(17) Threlfall, T. Structural and Thermodynamic Explanations of Ostwald's Rule. *Org. Process Res. Dev.* **2003**, *7*, 1017−1027.

(18) Zhang, T. H.; Liu, X. Y. Nucleation: What Happens at the Initial Stage? *Angew. Chem., Int. Ed.* **2009**, *48*, 1308−1312.

(19) Baletto, F.; Mottet, C.; Ferrando, R. Reentrant Morphology Transition in the Growth of Free Silver Nanoclusters. *Phys. Rev. Lett.* **2000**, *84*, 5544.

(20) Baletto, F.; Mottet, C.; Ferrando, R. Microscopic Mechanisms of the Growth of Metastable Silver Icosahedra. *Phys. Rev. B: Condens. Matter Mater. Phys.* **2001**, *63*, 155408.

(21) McHale, J. M.; Auroux, A.; Perrotta, A. J.; Navrotsky, A. Surface Energies and Thermodynamic Phase Stability in Nanocrystalline Aluminas. *Science* **1997**, *277*, 788−791.

(22) Chase, M. W.; Davies, C. A.; Downey, J. R.; Frurip, D. J.; McDonald, R. A.; Syverud, A. N. *NIST JANAF Thermochemical tables*; NIST Standard Reference Database 13; NIST: Gaithersburg, MD, 1985

(23) Shore, J. D.; Perchak, D.; Shnidman, Y. Simulations of the Nucleation of AgBr from Solution. *J. Chem. Phys.* **2000**, *113*, 6276−6284.

(24) Erdemir, D.; Lee, A. Y.; Myerson, A. S. Nucleation of Crystals from Solution: Classical and Two-Step Models. *Acc. Chem. Res.* **2009**, *42*, 621−629.

(25) Williams, S. R.; Royall, C. P.; Bryant, G. Crystallization of Dense Binary Hard-Sphere Mixtures with Marginal Size Ratio. *Phys. Rev. Lett.* **2008**, *100*, 225502.

(26) Lummen, N.; Kraska, T. Investigation of the Formation of Iron Nanoparticles from the Gas Phase by Molecular Dynamics Simulation. *Nanotechnology* **2004**, *15*, 525−533.

(27) Chakraborty, D.; Patey, G. N. How Crystals Nucleate and Grow in Aqueous NaCl Solution. *J. Phys. Chem. Lett.* **2013**, *4*, 573−578.

(28) Shen, T.; Meng, W.; Wu, Y.; Lu, X. Size Dependence and Phase Transition During Melting of fcc-Fe Nanoparticles: A Molecular Dynamics Simulation. *Appl. Surf. Sci.* **2013**, *277*, 7−14.

(29) Desgranges, C.; Delhommelle, J. Molecular Simulation of the Nucleation and Growth of Gold Nanoparticles. *J. Phys. Chem. C* **2009**, *113*, 3607−3611.

(30) Shibuta, Y.; Suzuki, T. A Molecular Dynamics Study of Cooling Rate During Solidification of Metal Nanoparticles. *Chem. Phys. Lett.* **2011**, *502*, 82−86.

(31) Al-Sunaidi, A. A.; Sokol, A. A.; Catlow, C. R. A.; Woodley, S. M. Structures of Zinc Oxide Nanoclusters: As Found by Revolutionary Algorithm Techniques. *J. Phys. Chem. C* **2008**, *112*, 18860−18875.

(32) Bromley, S. T.; Illas, F. Energetics and Structures of the Initial Stages of Nucleation of $(SiO_2)(N)$ Species: Possible Routes to Highly Symmetrical Tetrahedral Clustersw. *Phys. Chem. Chem. Phys.* **2007**, *9*, 1078−1086.

(33) Calatayud, M.; Maldonado, L.; Minot, C. Reactivity of $(TiO_2)(N)$ Clusters (N = 1−10): Probing Gas-Phase Acidity and Basicity Properties. *J. Phys. Chem. C* **2008**, *112*, 16087−16095.

(34) Qu, Z. W.; Kroes, G. J. Theoretical Study of the Electronic Structure and Stability of Titanium Dioxide Clusters $(TiO_2)(n)$ with n = 1−9. *J. Phys. Chem. B* **2006**, *110*, 8998−9007.

(35) Loschen, C.; Bromley, S. T.; Neyman, K. M.; Illas, F. Understanding Ceria Nanoparticles from First-Principles Calculations. *J. Phys. Chem. C* **2007**, *111*, 10142−10145.

(36) Burnin, A.; BelBruno, J. J. ZnnSm+ Cluster Production by Laser Ablation. *Chem. Phys. Lett.* **2002**, *362*, 341−348.

(37) Phipps, C. *Laser Ablation and Its Applications*; Springer Series in Optical Sciences; Springer: Berlin, 2007.

(38) Barcikowski, S.; Compagnini, G. Advanced Nanoparticle Generation and Excitation by Lasers in Liquids. *Phys. Chem. Chem. Phys.* **2013**, *15*, 3022−3026.

(39) Lam, J.; Amans, D.; Chaput, F.; Diouf, M.; Ledoux, G.; Mary, N.; Masenelli-Varlot, K.; Motto-Ros, V.; Dujardin, C. gamma-Al2O3 Nanoparticles Synthesised by Pulsed Laser Ablation in Liquids: A Plasma Analysis. *Phys. Chem. Chem. Phys.* **2014**, *16*, 963−973.

(40) de Heer, W. A. The Physics of Simple Metal Clusters: Experimental Aspects and Simple Models. *Rev. Mod. Phys.* **1993**, *65*, 611−676.

(41) Gardiner, W. C. *Gas-Phase Combustion Chemistry*; Springer: New York, 2000.

(42) Hahn, D. W.; Omenetto, N. Laser-Induced Breakdown Spectroscopy (LIBS), Part I: Review of Basic Diagnostics and Plasma-Particle Interactions: Still-Challenging Issues Within the Analytical Plasma Community. *Appl. Spectrosc.* **2010**, *64*, 335A−366A.

(43) Stewart, J. J. P. Optimization of Parameters for Semiempirical Methods I. Method. *J. Comput. Chem.* **1989**, *10*, 209−220.

(44) Sharipov, A. S.; Loukhovitski, B. I.; Starik, A. M. Theoretical Study of Structure and Physical Properties of $(Al_2O_3)_n$ Clusters. *Phys. Scr.* **2013**, *88*, 058307.

(45) Frisch, M. J.; Trucks, G. W.; Schlegel, H. B.; Scuseria, G. E.; Robb, M. A.; Cheeseman, J. R.; Scalmani, G.; Barone, V.; Mennucci, B.; Petersson, G. A.; et al. *Gaussian 09*, Revision D.01; Gaussian Inc.: Wallingford, CT, 2009.

(46) Patzer, A. B. C.; Chang, C.; Sedlmayr, E.; Sulzle, D. A Density Functional Study of Small AlxOy (x,y = 1−4) Clusters and their Thermodynamic Properties. *Eur. Phys. J. D* **2005**, *32*, 329−337.

(47) Li, R.; Cheng, L. Structural Determination of (Al2O3)(n) (n = 1−7) Clusters Based on Density Functional Calculation. *Comput. Theor. Chem.* **2012**, *996*, 125−131.

(48) McQuarrie, D. A.; Simon, J. D. *Molecular Thermodynamics*; University Science Books: Sausolito, CA, 1999.

(49) Lam, J.; Motto-Ros, V.; Misiak, D.; Dujardin, C.; Ledoux, G.; Amans, D. Investigation of Local Thermodynamic Equilibrium in Laser-Induced Plasmas: Measurements of Rotational and Excitation Temperatures at Long Time Scales. *Spectrochim. Acta, Part B* **2014**, *101*, 86−92.

(50) Ma, Q. L.; Motto-Ros, V.; Lei, W. Q.; Boueri, M.; Bai, X. S.; Zheng, L. J.; Zeng, H. P.; Yu, J. Temporal and Spatial Dynamics of Laser-Induced Aluminum Plasma in Argon Background at Atmospheric Pressure: Interplay with the Ambient Gas. *Spectrochim. Acta, Part B* **2010**, *65*, 896−907.

(51) Le Picard, S. D.; Canosa, A.; Travers, D.; Chastaing, D.; Rowe, B. R.; Stoecklin, T. Experimental and Theoretical Kinetics for the Reaction of Al with O-2 at Temperatures Between 23 and 295 K. *J. Phys. Chem. A* **1997**, *101*, 9988−9992.

(52) Pak, M. V.; Gordon, M. S. Potential Energy Surfaces for the Al +O-2 Reaction. *J. Chem. Phys.* **2003**, *118*, 4471−4476.

(53) Callard, S.; Masenelli, B.; Gagnaire, A.; Joseph, J. Dielectric Film Deposition for Optical Applications. *Vide-Sci. Technol. Appl.* **1999**, *54*, 58.

(54) Martinet, C.; Paillard, V.; Gagnaire, A.; Joseph, J. Deposition of SiO2 and TiO2 Thin Films by Plasma Enhanced Chemical Vapor Deposition for Antireflection Coating. *J. Non-Cryst. Solids* **1997**, *216*, 77−82.

(55) Pillonnet, A.; Pereira, A.; Marty, O.; Champeaux, C. Valence State of Europium Doping Ions During Pulsed-Laser Deposition. *J. Phys. D: Appl. Phys.* **2011**, *44*, 375402.

(56) Tainoff, D.; Masenelli, B.; Boisron, O.; Guiraud, G.; Melinon, P. Crystallinity, Stoichiometry, and Luminescence of High Quality ZnO Nanoclusters. *J. Phys. Chem. C* **2008**, *112*, 12623−12627.